Available online at www.sciencedirect.com
ScienceDirect
International Journal of Heat and Mass Transfer 51 (2008) 3153–3163
International Journal of HEAT and MASS TRANSFER
www.elsevier.com/locate/ijhmt

Experimental study of post-dryout with R-134a upward flow in smooth tube and rifled tubes

Song Kyu Lee *, Soon Heung Chang

Korea Advanced Institute of Science and Technology, 373-1, Guseong-dong, Yuseong-gu, Daejeon 305-701, Republic of Korea

Received 11 July 2007; received in revised form 18 August 2007
Available online 23 October 2007

Abstract

A study of post-dryout heat transfer was performed with a directed heated smooth tube and rifled tubes using vertical R-134a up-flow to investigate the heat transfer characteristics in the post-dryout region. Three types of rifled tube having different rib height and width were used to examine the effects of rib geometry and compare with the smooth tube, using a mass flux of 70–800 kg/m^2 s and a pressure of 13–24 bar (corresponding to an approximate water pressure of 80–140 bar). Wall temperature distribution in all tubes was strongly dependent on pressure and mass flux. Wall temperatures of the rifled tubes in the post-dryout region were much lower than for the smooth tube at same conditions. This was attributed to swirl flow caused by the rib. Thus, the thermal non-equilibrium, which is usually present in the post-dryout region, was lowered. The empirical correlation of heat transfer in the smooth tube of the post-dryout region was obtained. The heat transfer correlation for rifled tubes was also obtained as a function of rib height and width with the modification of the smooth tube correlation.

Keywords: R-134a; Post-dryout heat transfer; Empirical correlation; Critical quality; Rifled tube

1. Introduction

The post-dryout region in the tube is characterized by two-phase flow which transports liquid droplets in a continuous vapor flow, terminating in the superheated single-phase region. This post-dryout heat transfer mode has been called to the dispersed flow film boiling (DFFB). Significant thermal non-equilibrium between the liquid and vapor phases is usually present in DFFB regime, except for the high mass velocities. The post-dryout dispersed flow regime is encountered in applications, including once-through steam generators, boiling water reactors and pressurized water reactors during a loss-of-coolant accident.

Water cooled reactors generally operate with significant margin to dryout (burn-out condition). However, it is necessary to demonstrate fuel rod cladding temperatures within an allowable temperature range for certain postulated accidents. The post-dryout condition has to be avoided by design in recirculating boilers. Thus, an accurate prediction of wall temperature in the post-dryout dispersed region is of great importance. In once-through designs, however, dryout must occur at some location and the associated temperature increase must be accounted for the design. The post-dryout region exists in the heat exchanger operating in the once-through mode where the subcooled liquid enters the heat exchanger and the superheated vapor exits. The heat transfer mechanism that boils a fluid to saturated or superheated vapor can potentially benefit from heat transfer augmentation. Since the heated surface is mainly cooled by forced convection to vapor in the post-dryout region, the surface temperature can be increased to high temperature that is enough to damage to the heating surface due to a low heat transfer coefficient by the vapor flow. Hence, the studies of post-dryout heat

* Corresponding author. Tel.: +82 42 868 4248; fax: +82 42 861 4859.
E-mail addresses: sklee3@mail.kopec.co.kr (S.K. Lee), shchang@kaist.ac.kr (S.H. Chang).

0017-9310/$ - see front matter © 2007 Elsevier Ltd. All rights reserved.
doi:10.1016/j.ijheatmasstransfer.2007.08.026

Nomenclature

a_r	centrifugal acceleration (m/s^2)
d	inside diameter (m)
$dzchf$	distance from critical point (m)
E	electric voltage input (V)
G	mass flux (kg/m^2 s)
g	gravity acceleration (m/s^2)
h	rib height in rifled tube
I	electric current through test section (A)
k	thermal conductivity (kW/m °C)
L	lead length in rifled tube (m)
Nu	Nusselt number
P	pressure (bar)
q	heat flux (kW/m^2)
R	tube resistance (ohms)
r	inside radius in rifled tube (m)
Re	Reynolds number
Pr	Prandtl number
T	temperature (°C)
V_a	axial velocity (m/s)
V_{gf}	relative vapor velocity (m/s)
V_r	tangential velocity (m/s)
w	rib width in rifled tube (m)
x_a	actual quality
x_e	equilibrium quality
x_c	critical quality

Greek symbols

θ	acceleration ratio
ρ	density of fluid (kg/m^3)
σ	surface tension (N/m)
φ	helical angle of rib

Subscripts

l	liquid
R	rifled tube
S	smooth tube
sat	saturation
v	vapor
vf	vapor properties evaluated at film temperature $\left(\frac{T_w+T_b}{2}\right)$
w	wall

transfer on the once-through boiler as well as on accident analyses of light water reactors are necessary to prevent damage to the heating surface.

The numerous experiments and theoretical researches on post-dryout heat transfer have been conducted. Studies of post-dryout heat transfer using 3 × 3 and 5 × 5 rod bundles were performed by Unal et al. [1,2] and Kumamaru et al. [3], respectively. Unal et al. measured the vapor superheat using a vapor superheat probe and they concluded that most of the models, except Chen et al. (CSO), could not predict the wall heat flux, while all of the existing models could not predict the vapor superheat data or trends. Also, the studies of post-dryout heat transfer in tubes have been performed using various fluids, such as water, refrigerants. The experimental work of heat transfer in the post-dryout region of R-113 upward high quality flow in a uniformly heated tube was performed by Ueda et al. [4]. The analysis of heat transfer in the post-dryout region of up-flow in a uniformly heated tube on the basis of three path heat transfer model, involving heat transfer processes from wall to vapor, from vapor to liquid droplets and from wall to droplets in contact with the wall was performed by Koizumi et al. [5]. Their results were compared with a study by Ueda et al. [4], and they concluded that in the post-dryout region most part of heat from the tube wall is transferred to the vapor flow, while droplets impinging on the wall remove only a small part of heat.

In order to increase the heat transfer coefficients in the post-dryout region as well as CHF enhancement, some devices, such as ribbed tubes, various grooved tubes, twisters, springs and obstacles are used in the inside of tubes. Heat transfer augmentation in DFFB by tape generated swirl flow was studied by Bergles et al. [6] and France et al. [7]. Bergles et al. indicated that the heat transfer coefficients can be increased as much as 200% over the straight flow value at comparable conditions and the thermal non-equilibrium was minimized. Research of the post-dryout heat transfer at the rifled tube has not been performed. Many researches on single-phase heat transfer and CHF enhancement at rifled tube have been performed [8–11]. A study on the prediction of obstacle (rod spacing devices) effect on enhancement of film boiling heat transfer was performed by Leung et al. [12]. Devices such as rifled tubes, twisters, springs and grooves can be used to impose swirl or turbulent flows. An important two-phase flow regime in heat exchanger application is the post-dryout region, where heat transfer coefficients are considerably lower than coefficients for bubbly, slug or annular flow regimes occurring upstream of dryout. Of specific interest is post-dryout heat transfer where swirl or turbulent flow is generated by rifled geometry inside tubes. Studies of characteristics of smooth and rifled tubes in the post-dryout region were performed and compared with various mass flux and pressure conditions of R-134a. The rifled tube considerably increases the critical quality and lowers thermal non-equilibrium, improving heat transfer capability.

DFFB regime, a post-dryout heat transfer mechanisms, is usually occurred at void fractions in excess of 80% [13]. The following correlation for beginning of the dispersed regime was proposed by Levitan and Borevskiy [14]

$$x_{ad} = (2.7 \pm 0.3)\left(\frac{\rho_l \cdot \sigma}{G^2 \cdot d}\right)^{1/4}\left(\frac{\rho_v}{\rho_l}\right)^{1/3} \quad (1)$$

where x_{ad} represents the onset of annular dispersed flow.

Qualities calculated for the post-dryout region of present study exceed x_{ad}, thus considered as DFFB regime. The most important phenomena in DFFB are thermal non-equilibrium or vapor superheat. The heat is supposed to be transferred to Freon in DFFB regime by the two paths: convective heat transfer from the wall to the bulk vapor and convective heat transfer from the bulk vapor to the liquid droplets entrained in the vapor. The contribution to wall cooling by heat transfer from the wall to the liquid droplets is assumed to be noticeable only within short distances from the dryout point where the droplets have sufficient kinetic energy to impinge onto the wall [15]. The radiation heat transfer from the wall to the vapor and the liquid droplet in case of Freon is considered to be small due to low wall superheat. In the rifled tube, the swirl force induced by the rib causes the movement of droplets in the vapor toward the wall, and it will contribute to the heat transfer from the surface to liquid droplets which impact with the wall ('wet' collisions) or the heat transfer from the surface to liquid droplets which enter the thermal boundary layer but which do not wet the surface ('dry' collisions). Hence, the post-dryout heat transfer of the DFFB region in the rifled tube would be improved and decreased the wall temperature.

A large number of correlations have been developed for the heat transfer in DFFB regime. Equilibrium type correlations, which were empirically derived or assumed no non-equilibrium, include Dougall–Rohsenow [16], Condie–Bengston [17] and Groenveld [18]. These are variants of the single-phase Dittus–Boelter type correlation. The non-equilibrium type correlations, which attempt to predict the degree of non-equilibrium between the liquid and vapor phase, have been developed by Groeneveld and Delorme [19], Saha [20], Chen et al. (CSO) [21]. Most non-equilibrium correlations also use Dittus–Boelter type equations. This study focuses mainly on the effect of rifled geometry in heat transfer of the DFFB region and on the development of correlations for rifled tube effects. The correlation for the rifled tube is expressed as the modification of correlation for the smooth tube with a function of rib height and width. This correlation can be used to predict wall temperature in rifled tubes within parameter ranges of this study. The empirical correlation obtained with the smooth tube experimental results was compared to the CSO model [21] and the previous experimental data [25,26].

2. Experimental facility and test method

2.1. Experimental facility and test sections

A study on post-dryout heat transfer for smooth tube and rifled tubes were carried out in the R-134a thermal-hydraulic loop of Korea Advanced Institute of Science and Technology (KAIST). The heat transfer test apparatus of the KAIST R-134a experiment loop is schematically shown in Fig. 1 [22]. The R-134a experimental loop consists of a test section as a test tube, a mass flow meter, a pre-heater with a power of 25 kW for keeping the constant inlet subcooling, an accumulator for pressure control, a canned pump for R-134a mass supply, a condenser for cooling of R-134a, and a chilling system with R-22 and water–propylene glycol. The R-134a flow rate is controlled

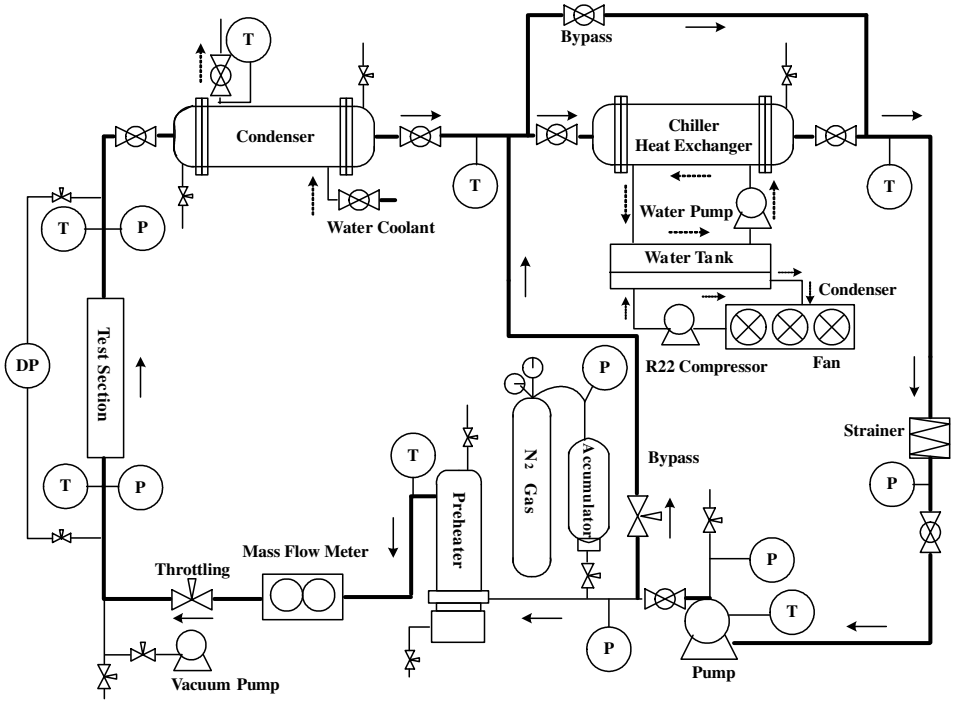

Fig. 1. Schematic diagram of the experimental system (*P*: pressure instrumentation, *T*: temperature instrumentation, DP: differential pressure instrumentation).

by adjustment of the motor speed of a canned pump and an adjusting valve in the inlet of test section is used to control flow rate to the test section. The loop is filled with R-134a in the vacuum condition of test section. The test loop is designed for a pressure of 30 bar and a temperature of 200 °C. Loop flow is measured by a mass flow meter calibrated to be 2% of RMS error by the manufacturer. Temperatures and pressures were measured at various locations as indicated by T and P, respectively, in Fig. 1.

The test section is schematically shown in Fig. 2 and is a carbon steel (SA192) tube with upward flow and a heated length of 3 m. The test tube is directly heated with a DC power supply, which controls the power by a power transformer with silicon controlled rectifiers (SCRs); the maximum power capacity is 40 V and 5000 A. The test section inlet of 150 mm was unheated to have fully developed condition of flow and the test section outlet of 200 mm was unheated to avoid the effect of cooling by flange and piping. The smooth tube had an average inner diameter of 17.04 mm and outside diameter of 22.59 mm; these dimensions were identical to the tube used in commercial boilers. The four-head spirally internally rifled tubes had a maximum inside diameter of 17.04 mm and outside diameter of 22.59 mm, and average volume-based inner diameters of 16.49 mm (Type A), 16.05 mm (Type B), 16.79 mm (Type C), respectively. The rib height of Type B rifled tube was largest among three rifled tubes and heights of Type A and C rifled tubes were same. The rib width of Type B rifled tube was largest, the medium width of Type A and the smallest width of Type C rifled tube. All rifled tubes had a spirally angle of 60°.

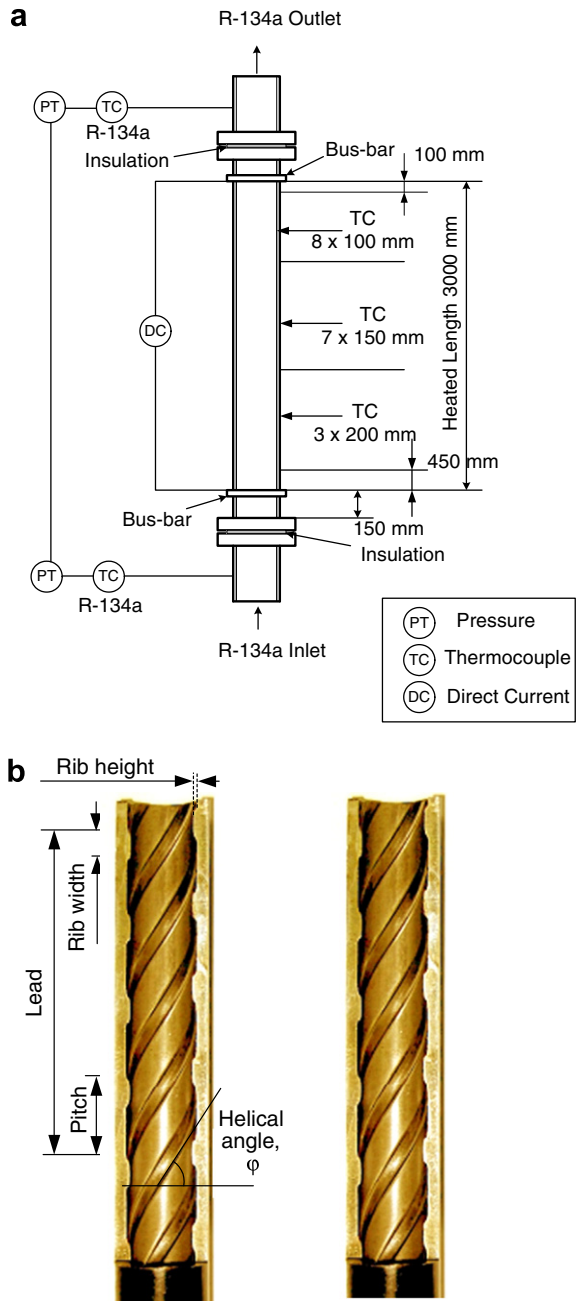

Fig. 2. Test section and rifled tube. (a) Test section and instrumentations and (b) typical cross-sectional view of rifled tube [22].

The test section was vertically installed in the test loop. Fluid temperatures at the inlet and outlet of the test section were measured with in-stream T-type sheathed thermocouples. Temperatures of the outside tube wall were measured at 18 locations along the channel wall; two thermocouples are installed apart 180° at each location along tube length with K-type thermocouples. Downstream thermocouples of the test section were installed more densely than upstream of the test section to measure the temperatures in the post-dryout region (Fig. 1). Outlet pressure and inlet pressure were measured with pressure transducers and calibrated to be 0.5% of RMS error for a full range. A pair of clamp-type copper electrodes grabs both ends of the test section. The test section was connected to the flange, which was insulated from other parts of the test loop with Teflon. The supplied current and the voltage difference between both ends of the test section were measured and collected by a data acquisition system.

2.2. Test procedure and test matrix

Post-dryout experiments were carried out for all test conditions. Single-phase heat transfer experiments with R-134a for both of smooth and rifled tubes were carried out to determine heat loss and check for heat balance and any abnormalities with the measuring instruments. Those results showed that heat losses were within 2.5%. After the pump starting, the mass flow was controlled by the speed control with the converter and the control valve at a certain level. The test pressure in the test loop was increased by turning on the pre-heater and increasing DC power to the test section. After the pressure in the test loop reached a pre-determined level, the inlet temperature was controlled by power control to the pre-heater. A pre-heater was used to keep a subcooled temperature of about 10 °C at inlet of test section for each test pressure. After setting the mass flow rate, inlet subcooling of about 10 °C, and

inlet pressure to the desired values, the electric power to test section was gradually increased in small steps.

The experimental conditions were: exit pressures of 13, 17 and 24 bar; mass fluxes between 70 and 800 kg/m^2 s; and average heat flux of between 24 and 240 kW/m^2. The system pressure was controlled by venting nitrogen gas in the accumulator and regulating the cooling water to the condenser. After reaching of CHF, the test parameters (mass flux, pressure, voltage and ampere of electric power supply, inlet temperature and wall temperatures at each power level) are stabilized for several minutes and recorded by a data acquisition system. This step continued until the maximum wall temperature did not exceed 500 °C to protect the test section from damage due to overheating. The test matrix and the equivalent water-based conditions were summarized in Table 1. The test conditions were selected by considering the startup condition of an once-through boiler of fossil power plant and the capacity of KAIST test loop.

2.3. Test data reduction

The volume-based inner diameter (d_{in}) of rifled tube was calculated:

$$d_{in} = \sqrt{\frac{4V}{\pi L}} \tag{2}$$

where V is the measured water volume required to fill a given length (L) of tube.

The inside tube wall temperatures were calculated from local heat generation and heat conduction through the wall:

$$T_{wi} = T_{wo} - \frac{q_Z d_{in}}{2k_w}\left(\frac{1}{2} - \frac{d_{in}^2}{d_{out}^2 - d_{in}^2}\ln\frac{d_{out}}{d_{in}}\right) \tag{3}$$

For rifled tubes, the volume-based inner diameter (d_{in}) is used in Eqs. (3) and (4). The mass flux measured in the flow meter for the rifled tube was corrected by the volume-based inner diameter (d_{in}) to represent the real flow situation. The average heat flux (q_E) of the test section was calculated:

$$q_E = \frac{EI}{\pi d_{in}} L_H \tag{4}$$

Since the tube resistance varied with the tube wall temperature, the heat generated in the tube was locally calculated in consideration of the variation of tube resistance by tube wall temperature. The resistance of carbon steel (SA192) was calculated as a function of temperature, thus the heat flux was not uniform along the direct heated test section. The local heat flux (q_Z) is calculated:

$$q_Z = q_E(R_Z/R_{REF}) \tag{5}$$

where R_Z is the carbon steel resistance at temperature of segment (Z), and R_{REF} is the carbon steel resistance at average tube temperature. The average tube temperature was calculated by summing the product of each segment temperature and segment length and then dividing by tube length.

After the local heat flux was determined, the thermodynamic equilibrium quality, the heat transfer coefficient based on the inside tube wall temperature and the saturation temperature were calculated along the test section length with the local heat flux. The thermophysical properties for R-134a were calculated by the NIST standard reference Database 23. Since the pressure drop along test section was negligible, the saturation temperature was based on pressure at the exit of test section.

Table 1
Test matrix

Test matrix condition in R-134a and water-equivalent conditions				
Pressure (bar)		Saturated temperature (°C)		Mass flux (R-134a), kg/m^2 s 70–800
R-134a	Water	R-134a	Water	Mass flux (water), kg/m^2 s
13	80	49.4	294.6	98.8–1129
17	102	59.2	310.6	98.4–1124
24	140	75.5	336.3	97.4–1113

3. Experimental results and discussion

3.1. Smooth tube

Fig. 3(a) and (b) shows the typical examples of wall superheated temperature at the inside tube surface in the post-dryout region of smooth tube as a function of equilibrium quality for the effects of mass flux and heat flux, respectively. The equilibrium quality in axial point is calculated with the local heat flux of tube segment which is generated by consideration of the tube resistance variation.

Fig. 3(a) shows the wall temperature sharply increased at the critical point followed by increasing wall temperature with a moderate gradient as the quality increase, and followed again by decreasing wall temperature. It is pronounced with increasing pressure and heat flux. The increasing wall temperatures in the upstream of post-dryout region can be explained by the factor that the vapor bulk temperature is increased due to low vapor heat transfer coefficients, where the convection heat transfer from wall to vapor is dominant and the heat transfer from vapor to droplet is negligible since the thermal non-equilibrium is not significant. Then, the wall temperature in the downstream of post-dryout region is decreased as the vapor velocity increases with increasing vapor quality by droplet evaporation. As the heat flux is increased, the critical point moves to lower quality and it is pronounced with increasing pressure.

Fig. 3(b) shows the pressure effect on the wall temperature. The wall temperature is decreased as the pressure increases at the mass flux of 290 kg/m^2 s, however the wall temperatures are not affected by the pressure at the mass flux of 700 kg/m^2 s. These can be explained in terms of a change in density ratio of R-134a. The density ratio (ρ_l/ρ_g) of R-134a sharply decreases with increasing pressure

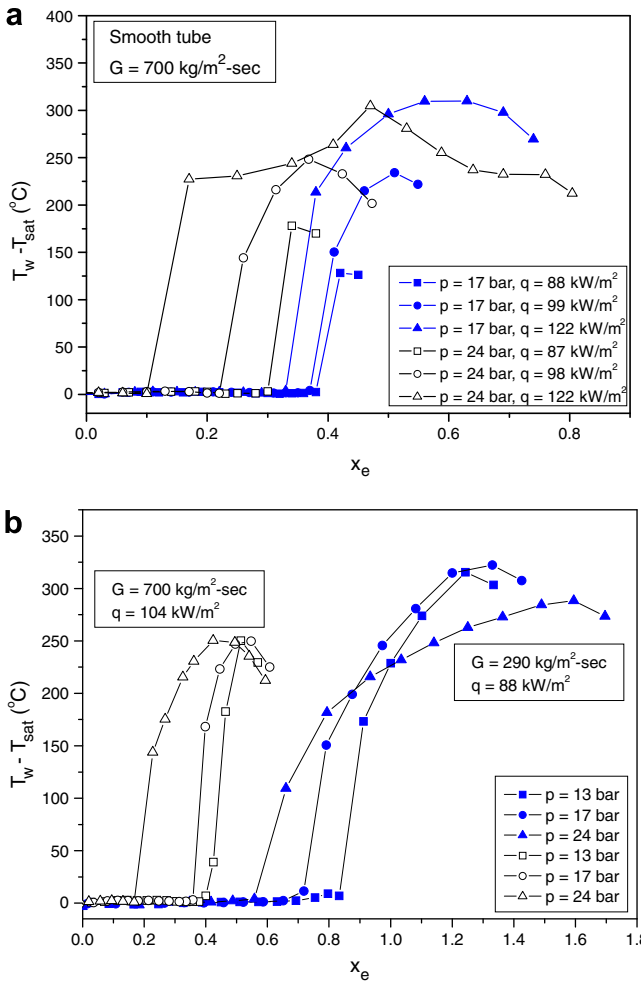

Fig. 3. Wall temperature distribution with quality in smooth tube at (a) 700 kg/m^2 s and (b) 13, 17 and 24 bar.

and it causes void fraction to decrease. The decrease of void fraction results in lower vapor superheat, hence low thermal non-equilibrium and better convective heat transfer from the wall. This effect is dominant with decreasing mass flux since the thermal non-equilibrium becomes significant and the void fraction larger. The other competing mechanism with increasing pressure is to decrease of vapor velocity by the decrease of density ratio, and it results in the decrease of convection heat transfer in DFFB region. However, the improvement of the heat transfer in DFFB regime with increasing pressure is mainly attributed to the lower thermal non-equilibrium between vapor and entrained droplets. Thus, the latter mechanism is less effective than the former mechanism. Fig. 3(b) also shows the critical point moves to lower qualities as the pressure increases.

3.2. Rifled tubes

Fig. 4(a)–(c) shows the wall temperature distribution between the smooth tube and the rifled tubes at the pressures of 13, 17 and 24 bar. The heat flux of smooth tube could not exceed the heat flux of 130 kW/m^2 to maintain the wall temperature below 500 °C for prevention of tube damage. The critical points at rifled tubes move to higher qualities against the smooth tube and it is pronounced with increasing pressure and mass flux. The wall temperatures at rifled tubes are considerably decreased against the smooth tube and it is also pronounced with increasing pressure and

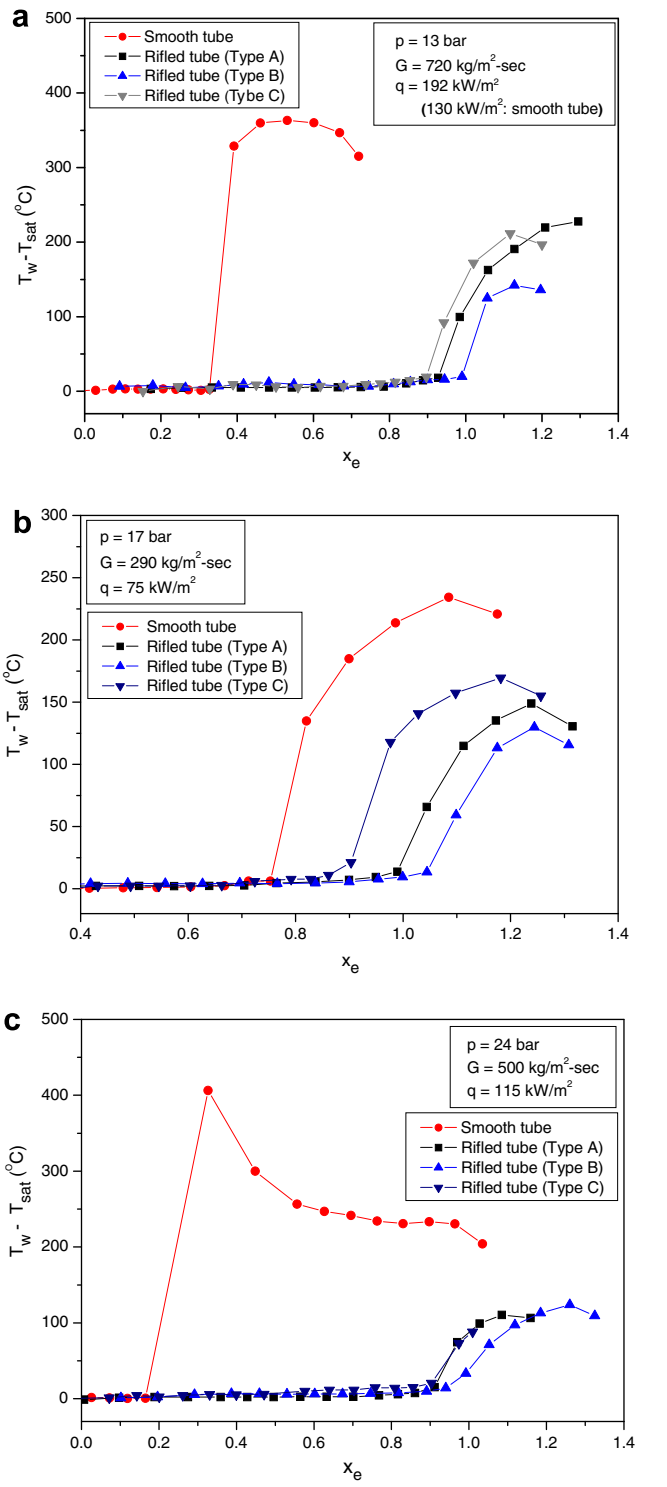

Fig. 4. Wall temperature distribution in a smooth tube and three rifled tubes at (a) 13, (b) 17 and (c) 24 bar.

mass flux. The rifle geometry effect is shown in the low mass flux and low pressure, but not shown in high pressure and high mass flux. This may be explained by the factor that the decrease of thermal non-equilibrium by the rifled tube is pronounced with decreasing pressure since the vapor drift force is increased with the decrease of pressure and mass flux. The results show Type B rifled tube is most effective for the decreasing of wall temperature and it can be interpreted that the rib height is effective for the increase of heat transfer in DFFB region. The wall temperature decrease at rifled tube is attributed to the effect of swirl flow due to the rib. The swirl flow forces the entrained droplets in vapor toward the tube wall and the heat transfer between wall and droplets is increased by both 'wet' and 'dry' collision, hence the thermal non-equilibrium is lowered and the wall temperature is decreased.

Fig. 5(a) shows the effects of mass flux and heat flux at the pressure of 17 bar in Type A rifled tube. As expected, the lower mass flux and higher heat flux result in the high wall temperatures, however the critical qualities are not nearly changed by mass flux and heat flux at same pressure. These results are different from that of the smooth tube (refer to Fig. 3). Fig. 5(b) shows the effects of pressure and heat flux in the Type A rifled tube at the mass flux of 750 kg/m^2 s. The effect of pressure on decreasing of wall temperatures is pronounced with increasing heat flux and the critical point moves to lower qualities at high pressure and high heat flux.

3.3. Critical quality and non-equilibrium in smooth tube and rifled tubes

Fig. 6(a) and (b) shows comparison of critical qualities between the smooth tube and the rifled tubes at the mass flux of 300 kg/m^2 s and 700 kg/m^2 s, respectively. The rifled tube effects on critical quality are much pronounced at high mass flux. As expected, the critical qualities are decreased at higher pressure and this trend is pronounced at the smooth tube and low mass flux. The critical quality for Type B rifled tube is lower than for Type A rifled tube and it is also pronounced at low mass flux. Fig. 7 shows the decreasing trend of critical qualities with increasing of

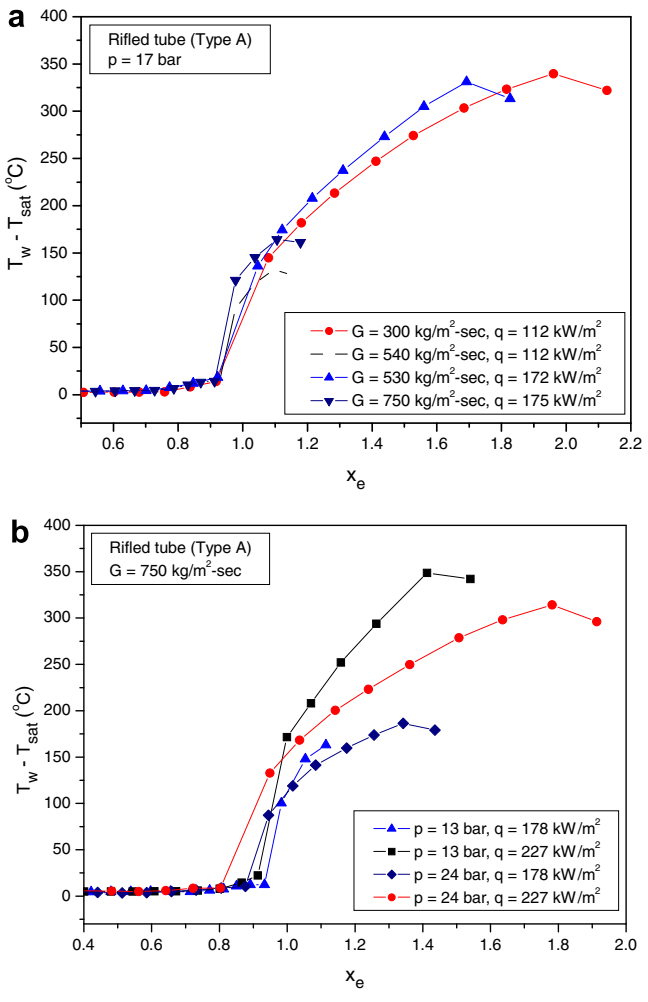

Fig. 5. Wall temperature distribution in a Type A rifled tube at (a) 17 bar and (b) 750 kg/m^2 s.

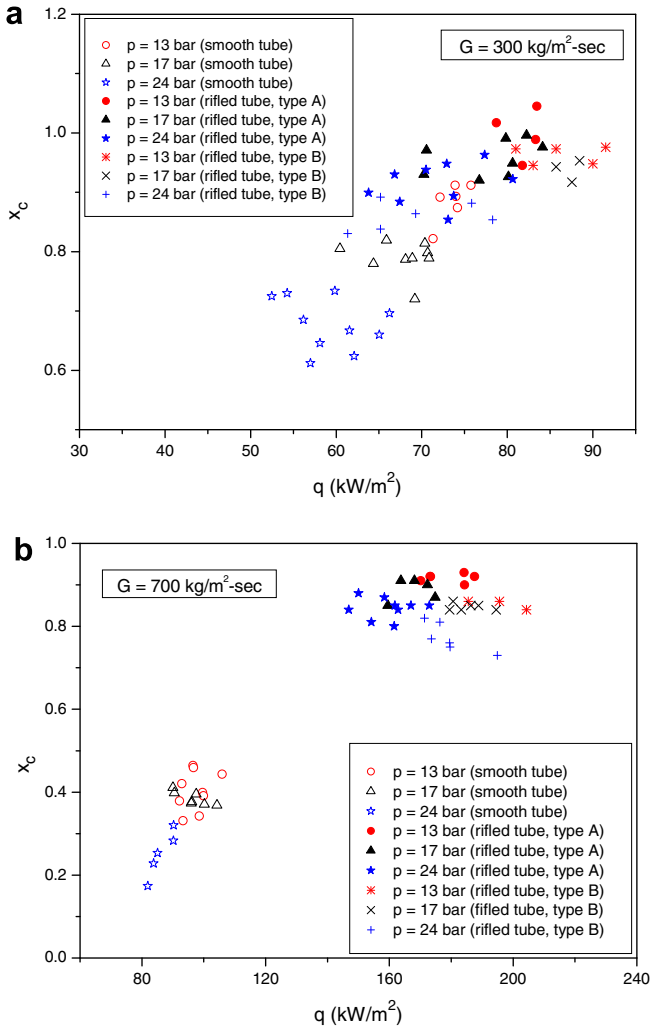

Fig. 6. Critical quality vs. heat flux in a smooth tube and two rifled tubes at mass flux of (a) 300 kg/m^2 s and (b) 700 kg/m^2 s.

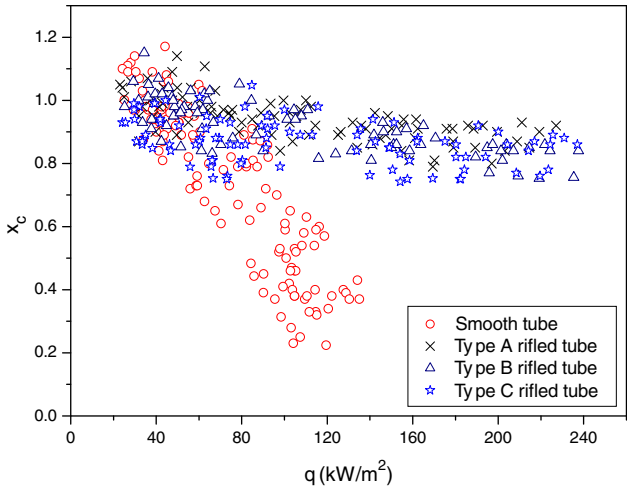

Fig. 7. Critical quality vs. heat flux in a smooth tube and three rifled tubes.

heat flux at the smooth tube and the rifled tubes. The critical qualities in the smooth tube steeply decrease with increasing of the heat flux.

A state of the thermal non-equilibrium between vapor and liquid phases is highly probable in DFFB and it is considered that the thermal non-equilibrium is decreased by the rifling. The improvement of heat transfer in rifled tubes is mainly attributed to swirl flow developed by the rib. It causes to disturb the thermal boundary layer and increase the heat transfer between the entrained droplets and the wall, and it results in the decrease of the thermal non-equilibrium. Fig. 8 shows the changes in actual qualities calculated by CSO correlation [21], which is best fit with the present test results, with the changes in equilibrium qualities from the present study. These results explain the decrease of non-equilibrium by rifled tubes. The diagonal line represents the equilibrium conditions, which the equilibrium quality and the actual quality are equal. The data for smooth tube are scattered far below from the equilibrium diagonal line, and it means that many non-equilibrium conditions exist. The non-equilibrium conditions are much decreased in rifled tubes.

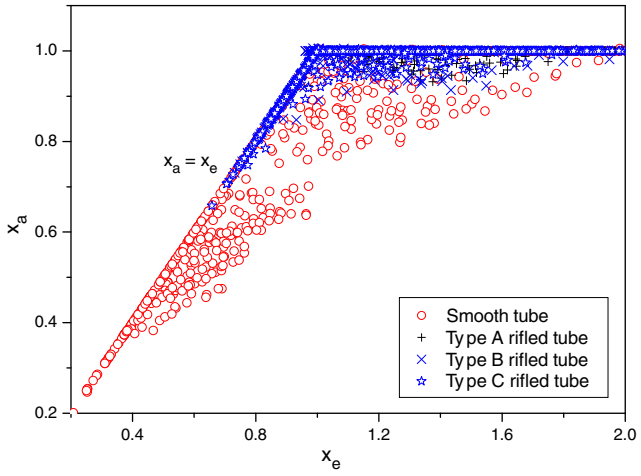

Fig. 8. Actual quality calculated by CSO model [21] vs. equilibrium quality in a smooth tube and three rifled tubes.

3.4. Correlations of post-dryout heat transfer for smooth tube and rifled tube

Table 2 shows the comparison of the predicted wall superheat by various correlations and measured wall temperature obtained in the present study. Some of correlations are thermal equilibrium model (Dougall–Rosenhow, Condie–Benngston) and some are thermal non-equilibrium model (Chen et al. (CSO), Groenveld–Delrome, Saha, Hein and Kohler). In non-equilibrium model, the actual quality and the vapor temperature are calculated and the post-dryout heat transfer coefficient is calculated based on the difference of wall and superheated vapor temperatures, while the heat transfer coefficient in equilibrium model is calculated based on the difference of wall and saturated vapor temperatures. The CSO correlation [21] shows the best prediction of wall temperature for the present experiment results with an average error of 2.2%. The prediction of Saha [20] and Hein and Kohler [23] models are not as accurate as the CSO correlation. The predictions by equilibrium models, Dougall–Rosenhow [16] and Condie–Bengston [17] fairly agree with the present experiment results and they predict the wall temperature with average errors of 4.4% and 9.2%, respectively. The study by Gottula [24] shows that Dougall–Rohsenow correlation produced the best overall fit with their experiment results. Fig. 9(a) shows the comparison of predicted wall superheat

Table 2
Wall temperature prediction in post-dryout region by existing correlations for smooth tube

Correlation	Average		RMS		Correlation type
	Deviation (°C)[a]	Error (%)[b]	Deviation (°C)[a]	Error (%)[b]	
Dougall–Rohsenow [16]	11.8	4.4	49.8	18.8	Equilibrium
Condie–Bengston [17]	24.3	9.2	46.4	17.5	Equilibrium
Chen et al. (CSO) [21]	5.7	2.2	35.5	13.4	Non-equilibrium
Groenveld–Delorme [19]	124.0	46.9	139.2	52.6	Non-equilibrium
Saha (k1 correlation) [20]	42.0	15.9	74.6	28.2	Non-equilibrium
Hein and Kohler [23]	42.2	16.0	77.2	29.1	Non-equilibrium
Present correlation	−5.4	−2.0	28.0	10.5	

[a] Statistics fit the wall temperature prediction – Deviation: d = predicted value − measured value; Avg. deviation = $\frac{1}{N}\sum_{i=1}^{N} d_i$, RMS deviation = $\sqrt{\frac{1}{N}\sum_{i=1}^{N} d_i^2}$, where N = no. of data.

[b] In the comparison of various correlations, the average and RMS error for the prediction is defined as: Error = (predicted value/measured value − 1); Avg. error = $\frac{1}{N}\sum_{i=1}^{N}(\text{error})_i$, RMS error = $\sqrt{\frac{1}{N}\sum_{i=1}^{N}(\text{error})_i^2}$, where N = no. of data.

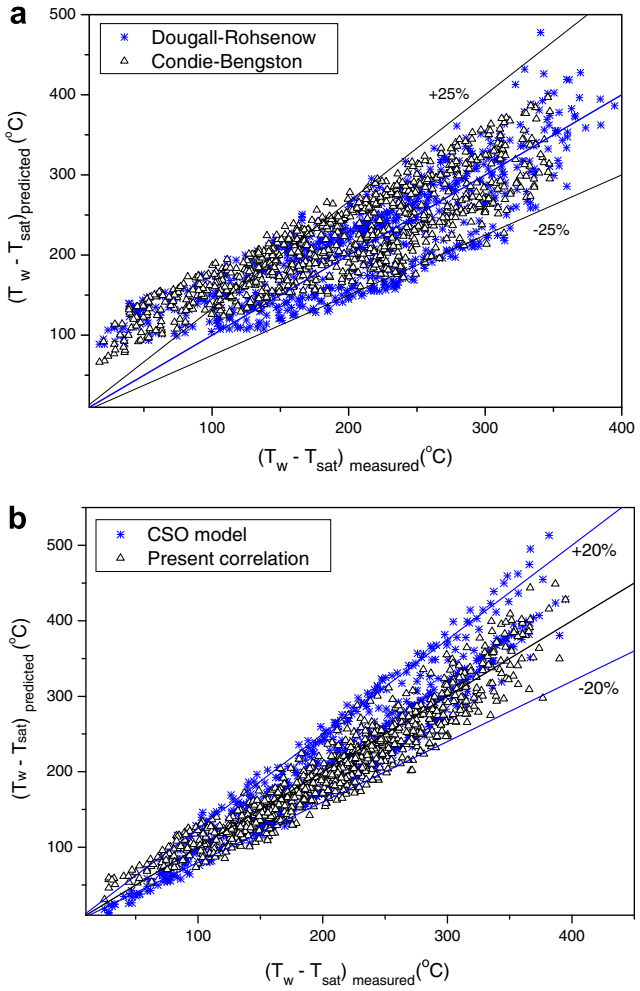

Fig. 9. Measured vs. predicted wall superheat in a smooth tube by (a) Dougall–Rohsenow [12] and Condie–Bengston [13] and (b) CSO [15] and present correlation in a smooth tube.

by Dougall–Rosenhow, Condie–Bengston and the measured wall superheat obtained in the present study. These explain that the equilibrium correlation may be used for the prediction of wall temperature under the present experimental conditions.

The empirical correlation on smooth tube is developed with the present experiment results, which the heat transfer coefficient was calculated based on the saturated vapor temperature and the inside tube wall temperature. The predicted wall superheat by the obtained correlation is shown in Fig. 9(b) with CSO correlation results and it agrees well with the prediction by CSO correlation. The following is the correlation obtained here with the present experiment results for the smooth tube:

$$Nu_S = 0.2935 \frac{x_c^{0.568}\left\{Re_v\left[x_e + \frac{\rho_v}{\rho_l}(1-x_e)\right]\right\}^{0.645} Pr_{vf}^{0.854}}{x_e^{0.715}\left(1+\frac{dzchf}{d}\right)^{0.088}} \quad (6)$$

The 923 data points were used for statistical fit and the empirical correlation was obtained from regression analysis. The correlation obtained for smooth tube predicts the wall temperature in the post-dryout region with the average error of −2.0% for data used in its development. The present correlation includes parameters of Re_v, Pr_{vf} which are thought to be important in DFFB heat transfer, and x_e accounting for the local variation of the heat flux, and x_c, $1+\frac{dzchf}{d}$ accounting for the influence of critical point hydraulics and distance from the critical point. Fig. 10 shows the comparison of existing published data having equal mass flux conditions with the present correlation results. Since the published data on post-dryout heat transfer with R-134a does not exist, the data for Freon 12 and 22 were used for the comparison of present correlation. The present correlation underestimates the wall temperature than the test results [25,26] and CSO model [21]. Fig. 11 shows the measured Nusselt numbers in three rifled tubes with Nusselt numbers equivalent to the smooth tube, which were calculated using the correlation (6) at the same condition with rifled tubes. It shows the post-dryout heat transfer in rifled tubes is increased by 40% in comparison with the smooth tube depended on the parameter conditions. The increase of heat transfer in rifled tubes is pronounced at higher heat transfer coefficients, which are conditions of high mass flux, high heat flux and low pressure. This can be explained by combined effects which cause to increase the relatively velocity of vapor; the swirl flow increase due to increase of tangential velocity by the rib at high mass flux and the increase of droplet drift toward the wall at low pressure due to large density difference between vapor and liquid. This trend of the heat transfer increase at rifled tubes can be explained by Eq. (8) below.

The swirl force moves the vapor toward the center of tube, the droplet toward the wall. An acceleration ratio is considered for the swirl effect as ratio of centrifugal acceleration to acceleration due to gravity [19]:

$$\theta = \frac{a_r}{g} = \frac{V_r^2}{r \cdot g} = \frac{V_a^2}{r \cdot g \tan(\varphi)^2} \quad (7)$$

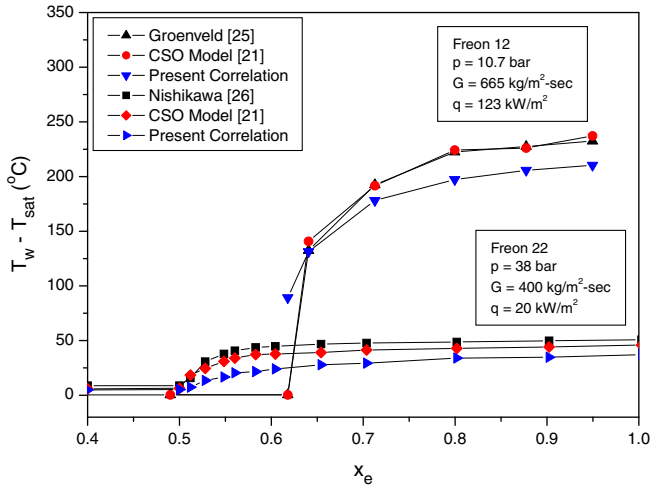

Fig. 10. Measured wall temperature vs. predicted wall temperatures by CSO model [21] and the present correlation in smooth tube.

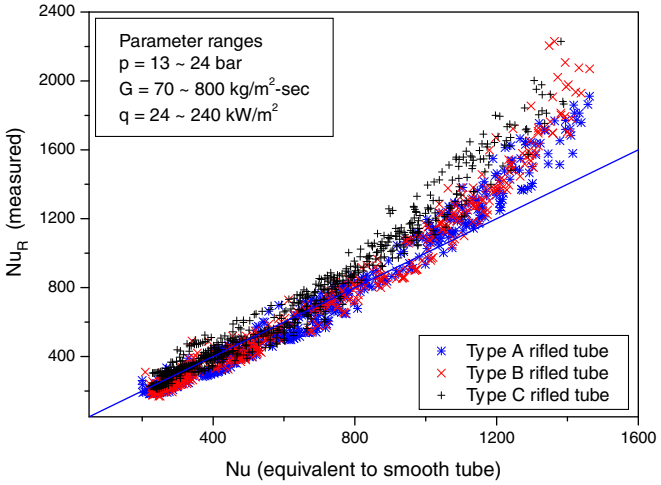

Fig. 11. Comparison of experimental *Nu* at rifled tube and predicted *Nu* equivalent to smooth tube by the present correlation.

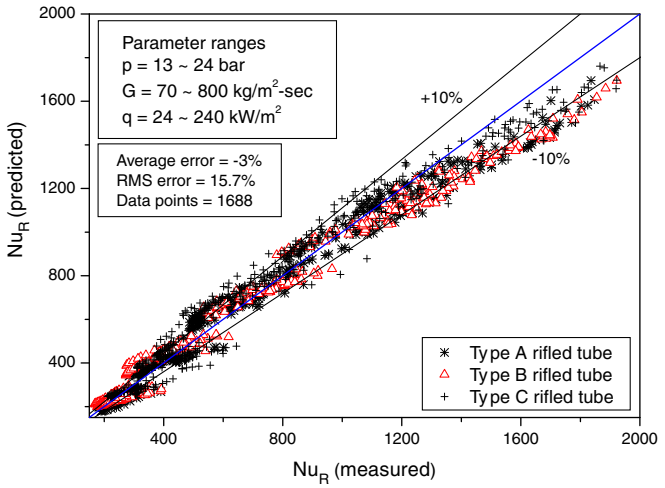

Fig. 12. Measured *Nu* vs. predicted *Nu* by the present correlation in three rifled tubes.

The heat transfer increase in rifled tubes is related to the relative velocity of vapor due to the centrifugal acceleration by swirl flow and it may be calculated [9] based on drift-flux model of two-phase flow:

$$V_{gf} = c\left[\frac{(\rho_f-\rho_g)\sigma\cdot a_r}{\rho_f^2}\right]^{1/4} = c\left[\frac{(\rho_f-\rho_g)\sigma}{\rho_f^2}\right]^{1/4}\times\left[\frac{V_a^2}{r\cdot g\tan(\varphi)^2}\right]^{1/4} \quad (8)$$

The rifling effects on heat transfer in DFFB region are dependent on the rib geometry. Hence, the correlation for heat transfer at rifled tube is developed with the parameters of rib geometry. The two geometry parameters, $\left(\frac{h}{d_{in}}\right)$, $\left(\frac{4w}{\pi d_{in}}\right)$ were considered in development of the heat transfer correlation for the rifled tube. Here, h is rib height and w is rib width. The rib number is four (4).

The 1688 data points for three types of rifled tube were used for statistical fit and the empirical correlation was obtained from regression analysis. The final correlation obtained from the present experiment results is as follows:

$$\frac{Nu_R}{Nu_S} = 0.6275\left\{Re_v\left[x_e+\frac{\rho_v}{\rho_l}(1-x_e)\right]\right\}^{0.123} \times Pr_{vf}^{-0.476}\left(\frac{h}{d_{in}}\right)^{0.562}\left(\frac{4w}{\pi d_{in}}\right)^{-0.269} \quad (9)$$

The heat transfer coefficients used in correlation development are calculated by the saturated vapor temperature and the inside tube wall temperature. The heat transfer coefficients (Nu_S) of smooth tube which are equivalent to rifled tube conditions were calculated by the correlation (6). The helical angle is important parameter for the performance of rifled tube, however it is not be shown in the correlation as well as the tube diameter because all data were taken with same helical angle and same tube diameter. The diameter was used to maintain non-dimensionality in the correlating parameter. Fig. 12 shows the measured Nusselt numbers and the predicted Nusselt numbers by the correlation (9) for the rifled tube and it predicts with the average error of −3% and the correlation underestimates at high Nusselt numbers.

4. Conclusions

The experiments for post-dryout heat transfer using R-134a in one smooth tube and three rifled tubes were performed. Based on this investigation, the following conclusions are obtained:

(1) The wall temperature in the post-dryout region at the rifled tube is far decreased than at the smooth tube and this effect is dominant at Type B rifled tube which has the higher rib. The wall temperature in the rifled tube as well as the smooth tube is dependent on mass flux and pressure, and the tube wall temperature is decreasing with increasing pressure.
(2) The rifling results in the critical point shift towards higher qualities and it is pronounced with increasing pressure and mass flux. The critical quality is more steeply decreased at the smooth tube with increasing of heat flux than at rifled tubes.
(3) There is the strong thermal non-equilibrium effect in the post-dryout region of smooth tube at the present experimental conditions. It is far lowered at rifled tube. The decrease of thermal non-equilibrium in rifled tubes is attributed to the effect of swirl and turbulent flow due to the rib, eventually decreased the wall temperature.
(4) Dougall–Rohsenow and Condie–Bengston equilibrium correlations show the reasonable predictions of tube wall temperature for the present experiment results. Chen et al. (CSO) non-equilibrium correlation produces the best overall fit with the present experiment results.

(5) The empirical thermal equilibrium correlations for heat transfer in the post-dryout region of smooth tube and rifle tubes were presented at the parametric range of $p = 13$–24 bar, $G = 70$–800 kg/m^2 s and the relatively high quality conditions. The correlation presented for smooth tube has the regression fit with the average error of -2.0% for data used in its development. It underestimates the wall temperature in comparison of the published experimental data. The post-dryout heat transfer correlation obtained for rifled tube has the regression fit with the average error of -3% and it shows that the post-dryout heat transfer in rifled tube can be increased by 40% than in the smooth tube.

(6) This research provides an insight into the post-dryout heat transfer enhancement of rifled tube through new correlation presented for post-dryout heat transfer. For the accurate prediction of wall temperature in the post-dryout region, it is necessary to supplement the correlations obtained here by considering a thermal non-equilibrium at high quality condition with direct measurement of the vapor superheat.

References

[1] C. Unal, K. Tuzla, J.C. Chen, S. Neti, O. Badr, Convective film boiling in a rod bundle: axial variation of non-equilibrium evaporation rates, Int. J. Heat Mass Transfer 31 (1988) 2091–2100.

[2] C. Unal, K. Tuzla, A.F. Cokmez-Tuzla, J.C. Chen, Vapor generation rate model for dispersed drop flow, Nucl. Eng. Des. 125 (1991) 161–173.

[3] H. Kumamaru, Y. Koizumi, K. Tasaka, Investigation of pre- and post-dryout heat transfer of steam-water two-phase flow in a rod bundle, Nucl. Eng. Des. 102 (1987) 71–84.

[4] T. Ueda, H. Tanaka, Y. Koizumi, Dryout of liquid film in high quality R-113 upflow in a heated tube, in: Proceedings of the 6th International Heat and Transfer Conference, Paper No. FB-26, Toronto, 1978.

[5] Yasuo Koizumi, Tatsuhiro Ueda, Hiroaki Tanaka, Post dryout heat transfer to R-113 upward flow in a vertical tube, Int. J. Heat Mass Transfer 22 (1979) 669–678.

[6] A.E. Bergles, W.D. Fuller, S.J. Hunek, Dispersed flow film boiling of nitrogen with swirl flow, Int. J. Heat Mass Transfer 14 (1971) 1343–1354.

[7] D.M. France, W.J. Minkowycz, C. Chang, Analysis of post-CHF swirl flow heat transfer, Int. J. Heat Mass Transfer 37 (suppl. 1) (1994) 31–40.

[8] W. Kohler, W. Kastner, Heat transfer and pressure loss in rifled tubes, in: Proceedings of the 8th International Heat Transfer Conference, San Francisco vol. 5, 1986, pp. 2861–2865.

[9] J. Weisman, J. Lan, P. Disimile, Two-phase (air–water) flow patterns and pressure drop in the pressure of helical wire ribs, Int. J. Multiphase Flow 20 (5) (1994) 885–899.

[10] L. Cheng, T. Chen, Flow boiling heat transfer in a vertical spirally internally ribbed tube, Heat Mass Transfer 37 (2001) 229–236.

[11] L. Cheng, G. Xia, Experimental study of CHF in a vertical spirally internally ribbed tube under the condition of high pressures, Int. J. Therm. Sci. 41 (2002) 396–400.

[12] L.K.H. Leung, D.C. Groeneveld, J. ZangYasuo Koizumi, Prediction of the obstacle effect on film-boiling heat transfer, Nucl. Eng. Des. 235 (2005) 687–700.

[13] D.C. Groeneveld, Post-dryout heat transfer: physical mechanisms and a survey of prediction methods, Nucl. Eng. Des. 32 (1975) 283–294.

[14] L.L. Levitan, L. Ya. Borevsky, Holographia steam-water flow, Moscow Energoatomizdat, 1989.

[15] M. Andreani, G. Yadigaroglu, Prediction methods for dispersed flow film boiling, Int. J. Multiphase Flow 20 (suppl.) (1994) 1–51.

[16] R.S. Dougall, W.M. Rohsenow, Film boiling on the inside of vertical tubes with upward flow of the fluid at low qualities, MIT Report No. 9079-26, Massachusetts Institute of Technology, 1963.

[17] K.G. Condie, S.J. Bengston, S.L. Richlein, Measurement of axially varying non-equilibrium in post-critical heat flux boiling in a vertical tube, NUREG/CR-3362, US Nuclear Regulatory Commission, 1983.

[18] D.C. Groenveld, Post-dryout heat transfer at reactor operating conditions, AECL-3281, Atomic Energy of Canada Limited, 1973.

[19] D.C. Groenveld, G.G.J. Delorme, Prediction of thermal non-equilibrium in the post-dryout regime, Nucl. Eng. Des. 36 (1976) 17–26.

[20] P. Saha, A non-equilibrium heat transfer model for dispersed droplet post-dryout regime, Int. J. Heat Mass Transfer 23 (1980) 483–492.

[21] J.C. Chen, F.T. Ozkaynak, R.K. Sundaram, Vapor heat transfer in post-CHF region including the effect of thermodynamic non-equilibrium, Nucl. Eng. Des. 51 (1979) 143–155.

[22] C.H. Kim, I.C. Bang, S.H. Chang, Critical heat flux performance for flow boiling of R-134a in vertical uniformly heated smooth tube and rifled tubes, Int. J. Heat Mass Transfer 48 (2005) 2868–2877.

[23] D. Hein, W. Kohler, A simple-to-use post-dryout heat transfer model accounting for thermal non-equilibrium, in: First International Workshop on Fundamental Aspects of Post-dryout Heat Transfer, Salt Lake City, UT, USA NUREG/CP-0060, 2–4 April 1984.

[24] R.C. Gottula, K.G. Condie, R.K. Sundaram, S. Neti, J.C. Chen, R.A. Nelson, Forced convective, non-equilibrium, post-CHF heat transfer experiment data and correlation comparison report, NUREG/CR-3193, March 1985.

[25] D.C. Groenveld, The thermal behavior of a heated surface at and beyond dryout, AECL-4309, 1972.

[26] K. Nishikawa, S. Yoshida, H. Mori, H. Takamatsu, An experiment on the heat transfer characteristics in the post-burnout region at high subcritical pressure, Nucl. Eng. Des. 74 (1982) 233–239.